RSC Advances

PAPER

View Article Online
View Journal | View Issue

Cite this: *RSC Adv.*, 2026, **16**, 25094

First principles rationale of strain-induced modifications in hybrid double halide perovskite: optoelectronics and photovoltaic perspectives

Tanmoy Kalita, Manjet Rajak and Dhruba Jyoti Kalita *

Received 19th March 2026
Accepted 5th May 2026

DOI: 10.1039/d6ra02285e

rsc.li/rsc-advances

Strain engineering enables precise tuning of optoelectronic properties by altering structural design, energy levels, and band gaps through tensile or compressive strain in various directions. While tensile strain promotes ion migration by weakening bonds and lowering activation energy, applying external compressive strain can offset residual tensile strain in perovskite films, enhancing their efficiency and stability. In this study, we have explored the impact of strain on the optoelectronic and photovoltaic properties of $(DMA)_2SnCl_6$ [DMA = dimethylammonium ($(CH_3)_2NH_2$) cation] employing density functional theory (DFT). Strain levels of 2%, 4%, and 6% have been applied in both tensile and compressive modes. Notably, the band gap decreases with increasing strain, irrespective of type. Mechanical property analysis confirms the compound meets most Born stability criteria, ensuring structural integrity. A maximum efficiency of 29.28% under 6% tensile strain along the *x*-axis underscores the potential of strain engineering to enhance photovoltaic performance.

1 Introduction

Perovskite solar cells are an emerging low-cost technology with the potential to surpass or coexist alongside silicon solar cells in the market. The most remarkable feature of perovskite materials in the photovoltaic community is their impressive increase in power conversion efficiency (PCE), rising from 3.8% to 22.7%.[1] Halide perovskite materials are employed as light harvesting materials with their wide application in the field of photo detectors, lasers and others. Though lead halide perovskites have emerged in the field of photovoltaics with PCE up to 22.1%, but they are poisonous and cause hazard to the environment. Therefore, there is demand to develop lead-free perovskite materials as environmental friendly alternatives. There are many ways to make the perovskites lead-free by replacing with the benign materials like isovalent Sn^{2+} ions. For predicting the electronic properties of newly designed materials, band gap plays an important key factor because it shows the exact positions of the active elements in the valence and conduction bands. In this regard, strain engineering is a sophisticated material technology which strongly affects the structural scheming, mechanical stability, energy level positions and band gap values, which enable us to manipulate the optoelectronic properties. Strain results in the alteration of the lattice parameters. Thus, the strain (e) can be defined as the ratio of the change in the lattice parameter (Δa) to the original, unaltered lattice parameter (a_0), and it is calculated using eqn (1):[2]

$$e = \frac{\Delta a}{a_0} \quad (1)$$

Strain engineering involves both tensile and compressive in the form of uniaxial, biaxial, or triaxial strain where tensile strain make the material elongated, weakens the chemical bonds, forms deep defect states, lowering the activation energy and enhances the ion migration. Nonetheless, it is possible to compensate for the remaining tensile strain in perovskite films by introducing external compressive strain, which enhances efficiency and stability by raising the activation energy for ion migration.[2]

Javed *et al.* looked into the effects of biaxial strains of 2%, 4%, 6%, and 8% on the second monolayer of phenylamoniumtiniodide (PH_2SnI_4) perovskites. DFT is used to study the mechanical stability, band gap tuning, octahedral tilting, structural distortion, and Bader charge analysis of the final configuration. After examination, all the constructions were found to be mechanically stable. The covalently connected structure is ductile, with a prominent stretching mode, under tensile or compressive mode.[2] Wu *et al.* examined the cause of strain in perovskites and how these affect the physical characteristics of materials and photovoltaic devices. Ultimately, they offer a viewpoint on how strain engineering might be used to advance the development of stable, highly effective perovskites.[3] Liu *et al.* investigated the causes of strain on FA-based perovskites and offers methods to alter lattice strain. The purpose of this review is to clarify how strain affects FA-based perovskites, identify viable strain engineering techniques to improve performance, eventually make it easier for these materials to be

Department of Chemistry, Gauhati University, Guwahati-781014, India. E-mail: dhrubajyoti.kalita@gauhati.ac.in

commercialized.[4] Shai *et al.* reviewed the origins, effects, and control of strain in metal halide perovskites, highlighting its impact on physical properties and solar performance. Their comprehensive analysis promotes interest in strain engineering to enhance performance and stability, supporting the commercialization of perovskite photovoltaics.[5] Moreover, Rahman *et al.* reported a comprehensive first-principles investigation of the strain-dependent electronic and optical properties of inorganic Sr_3PI_3 perovskite, emphasizing its potential for photovoltaic applications. Their density functional theory calculations, including spin-orbit coupling (SOC) effects, revealed a direct bandgap at the Γ-point, with a slight reduction upon incorporation of relativistic effects. The study demonstrated that compressive strain induces bandgap narrowing, whereas tensile strain leads to bandgap widening, indicating effective bandgap tunability through strain engineering. These electronic modifications were shown to significantly influence the optical response, resulting in strong visible-light absorption and strain-induced red-shift or blue-shift behavior in the dielectric function and absorption spectra. Furthermore, device simulations using the SCAPS-1D framework predicted high photovoltaic performance for Sr_3PI_3-based solar cells employing SnS_2 as the electron transport layer (ETL), highlighting the promise of strain-engineered Sr_3PI_3 for optoelectronic and photovoltaic applications.[6] Similarly, Islam *et al.* explored the strain-dependent electronic, optical, and mechanical properties of lead-free Ca_3PCl_3 inorganic perovskite using first-principles density functional theory. Their study showed that Ca_3PCl_3 is a direct-bandgap material whose bandgap can be effectively tuned by biaxial strain, with compressive and tensile strains inducing red-shift and blue-shift behavior, respectively, in the optical spectra. The material was also reported to exhibit good mechanical stability and ductility under strain, highlighting its potential for strain-engineered photovoltaic and optoelectronic applications.[7]

In parallel, pressure engineering has been shown to effectively modulate perovskite properties. For instance, Cs_2PdBr_6 retains structural stability under hydrostatic pressure while exhibiting enhanced mechanical properties and reduced bandgap, leading to improved optical absorption and conductivity.[8] Likewise, $CsGeI_3$ demonstrates an optimal bandgap ($\sim$1.37 eV) under slight negative pressure (-0.5 GPa), along with enhanced dielectric response, carrier transport, and optical absorption, confirming its potential for photovoltaic applications.[9]

Building on this literature survey, a clear research gap remains in the systematic investigation of strain effects in hybrid organic–inorganic double halide perovskites, which have received comparatively less attention than their fully inorganic counterparts despite their potential advantages in stability and tunability. While existing studies demonstrate that both strain and pressure effectively modulate band structure, optical response, and mechanical properties in inorganic and simple hybrid systems, comprehensive analyses of hybrid double perovskites, where organic cations introduce additional structural flexibility, dielectric screening, and defect tolerance are still lacking. In particular, the role of organic components in mediating strain-induced electronic transitions, octahedral distortions, and overall optoelectronic performance remains insufficiently understood, thereby motivating further investigation in this class of materials.

Motivated by these gaps and the growing demand for environmentally benign photovoltaic materials, the present study systematically investigates the strain-dependent mechanical, optoelectronic, and photovoltaic properties of the lead-free hybrid double halide perovskite: $(DMA)_2SnCl_6$. The primary purpose of choosing lead-free double halide perovskite for this investigation is because they are safer alternative for environmental and health concerns.[10–12] Moreover, these kinds of materials exhibit higher stability under ambient conditions and high-intensity illumination compared to lead halide perovskites.[10,11] Strain was applied to the material at levels of 2%, 4%, and 6% through both tensile and compressive modes. To assess the impact of variable strain on the electronic properties, we have calculated the band gap (E_g) values for the selected material with the respective strain percentage. For further study of the optical and photovoltaic properties, we have evaluated the real and imaginary parts of complex dielectric function(ε), absorption coefficients (α), open circuit voltage (V_{oc}), short-circuit current density (J_{sc}) and the theoretical power conversion efficiency (η), respectively.

In first-principles simulations, externally applied strain is commonly restricted to small magnitudes in order to probe the elastic deformation regime, where lattice distortions are reversible and the crystal symmetry remains intact. Within this regime, strain primarily modifies bond lengths and bond angles, leading to systematic shifts in band edges and bandgap values without inducing plastic deformation or phase transitions. Consequently, analyzing material properties under controlled elastic strain provides physically meaningful insights into structure–property relationships relevant for device applications.[2,13]

2 Computational methodology and theoretical details

The first principle calculations have been performed within the framework of DFT using the plane wave pseudopotential approach (PWSCF) as implemented in the QUANTUM ESPRESSO software package (QE).[14] The crystallographic information files are collected from the free databases of crystal structures such as Crystallography Open Database[15] and Materials Project.[16]

To validate the applied methodology, initially self-consistent field (SCF) computations have been carried out using an experimentally reported compound, $Cs_2AgBiCl_6$. This compound was chosen because it shares a similar architecture to the designed compound being studied, making it an appropriate reference for comparison. Five different types of exchange–correlation (XC) functionals have been employed to ensure a comprehensive evaluation: local density approximation (LDA),[17] Perdew–Burke–Ernzerhof (PBE),[18] PBE0,[19] Perdew–Burke–Ernzerhof revised for solids (PBEsol),[20] and the Heyd–

Scuseria–Ernzerhof hybrid functional (HSE06).[21] It is well established that GGA-based functionals, including PBE, generally tend to underestimate electronic band gaps due to their approximate treatment of exchange–correlation effects.[22–24] Although the comparative results summarized in Table S1 of SI, reveal that the PBE XC functional shows the closest agreement with the experimentally reported value (experimental band gap = 2.2 eV) for this compound,[25,26] such agreement may arise from error cancellation rather than intrinsic accuracy. In contrast, hybrid functionals such as HSE06 generally provide improved absolute bandgap values, as demonstrated in prior studies on halide perovskites.[26–28]

Nevertheless, GGA functionals such as PBE are widely recognized to reliably capture the qualitative features of electronic structure and, importantly, the relative trends induced by external perturbations such as strain. Therefore, in the present work, PBE is employed as a computationally efficient and internally consistent framework to investigate strain-dependent variations in electronic and optical properties. The conclusions are thus based on relative changes in band structure, while the absolute values of derived photovoltaic parameters (*e.g.*, open-circuit voltage and power conversion efficiency) should be interpreted with appropriate caution due to the known limitations of the PBE functional.

A 2 × 2 × 2 Monkhorst–Pack grid of *k*-points along with PAW (Projector-Augmented Wave) pseudopotentials (PPs) are used for both geometry optimization and SCF calculations. During the calculations, the kinetic-energy and the charge density cutoff is set to 47 and 470 Ry, respectively. The intended structures are fully relaxed until the residual forces on atoms converged below 0.001 Ry per Bohr. The excited state calculations have been performed by using time-dependent density functional theory (TD-DFT) formalism embodied in the QE program package.[29] Besides that, to investigate the optical properties of our designed compound under varying strain level, we have calculated real (ε_1) and imaginary (ε_2) parts of complex dielectric functions (ε) using norm-conserving pseudopotentials. Further, to investigate the optical absorption properties, we have calculated the absorption coefficients using the complex dielectric functions.[29]

Apart from that, to investigate the photovoltaic properties of the selected compound, we first present an idealized bandgap-based estimation of key parameters such as V_{oc}, J_{sc} and η for reference. The short-circuit current density (J_{sc}) can be expressed as:[30,31]

$$J_{sc} = e\int_{E_g}^{\infty} \frac{S(E)}{E}\mathrm{d}(E), \tag{2}$$

where, e is the electronic charge, E is the incident energy of a photon and $S(E)$ is the incident spectral power per unit area. This expression utilizes the AM1.5G solar spectrum provided by the national renewable energy laboratory (NREL).[31]

Moreover, V_{oc} can be estimated on the basis of the fundamental band gap, E_g of the material and a variable parameter called loss-in-potential, E_{loss} as shown in eqn (3),

$$eV_{oc} = E_g - E_{loss}. \tag{3}$$

Here, we have considered two values of E_{loss} *viz.* 0.7 and 0.5 eV as suggested by the previously reported literature.[30,31]

The maximum theoretical PCE (η) of hybrid perovskites can be calculated using the values of J_{sc} and V_{oc} as shown in eqn (4),

$$\eta = \frac{\mathrm{FF} \times J_{sc} \times V_{oc}}{P_{sun}}, \tag{4}$$

where, FF stands for fill factor and P_{sun} is the total incident power. P_{sun} can be calculated by using eqn (5) as shown below,

$$P_{sun} = e\int_0^{\infty} S(E)\mathrm{d}(E). \tag{5}$$

However, this approach assumes complete absorption of photons above the band gap and ideal carrier collection, and therefore may significantly overestimate the photovoltaic performance. To obtain a more realistic estimation, the photovoltaic performance of the studied compound has been evaluated using the spectroscopic limited maximum efficiency (SLME) approach, implemented *via* the SL3ME.py code[32] (The source code is publicly available at: https://github.com/ldwillia/SL3ME). In this framework, the calculated band gap values are used together with the absorption coefficient (α) and film thickness to determine the optical absorption and recombination characteristics of the material. The wavelength-dependent absorbance is evaluated using the Beer–Lambert relation, $A(\lambda) = 1 - \exp(-2\alpha(\lambda)t)$, thereby accounting for incomplete absorption across the solar spectrum. The absorption profile is combined with the AM1.5G solar spectrum to compute the photogenerated current through numerical integration of the photon flux. In addition, radiative recombination losses are included *via* the evaluation of the reverse saturation current density (J_0) using detailed balance principles. The current–voltage (J–V) characteristics are then constructed, and the maximum output power is obtained through numerical optimization, from which the power conversion efficiency (η) is determined.

However, it should be noted that $(DMA)_2SnCl_6$ is a vacancy-ordered double perovskite with a 0D electronic structure consisting of spatially isolated $[SnCl_6]^{2-}$ octahedra. Such systems typically exhibit carrier localization, weak band dispersion, relatively large effective masses, and strong excitonic effects, which can hinder efficient charge separation and transport. Therefore, although the SLME approach provides a more realistic estimate, it does not explicitly account for exciton binding or non-radiative recombination processes. As a result, the calculated efficiency values should be interpreted as an idealized upper bound, and the actual device performance may be significantly lower.

3 Results and discussion

3.1 Structural details

The selected compound $((CH_3)_2NH_2)_2SnCl_6$ crystallizes in orthorhombic crystal phase having space group *Pnnm*. The structure of the compound consists of four $(CH_3)_2NH_2$ and two $SnCl_6$ clusters. In $(CH_3)_2NH_2$, the N atom is bonded in

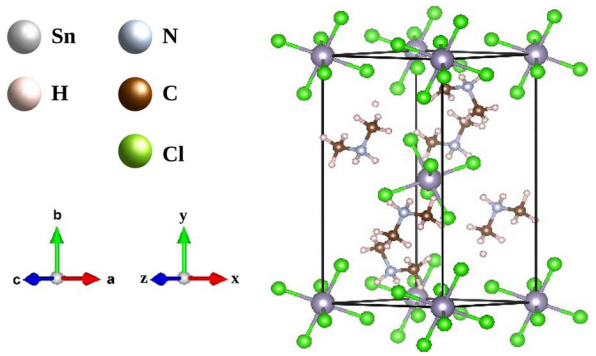

Fig. 1 Optimized structure of $((CH_3)_2NH_2)_2SnCl_6$ without applying external strain.

a distorted tetrahedral geometry to two C and two equivalent of H-atoms. The C–N, C–H, and N–H bond lengths are of 1.49 Å, 1.09 Å, and 1.04 Å, respectively. In addition, the axial and equatorial Sn–Cl bonds of $SnCl_6$ clusters are of the length of 2.47 Å. The optimized structure of $((CH_3)_2NH_2)_2SnCl_6$ is provided in Fig. 1. In addition, the lattice parameters of $((CH_3)_2NH_2)_2SnCl_6$ along with the unit cell volumes at different percentile of tensile and compressive strains are provided in Table 1 and 2, respectively.

3.2 Electronic properties

3.2.1 Band gaps (E_g) and band structures. To investigate the electrical characteristics of the selected compound on varying strain levels, we have computed the fundamental band gap (E_g) values, which are shown in Tables 3 and 4, respectively. Tables 3 and 4 manifest that except for the 6% tensile strain along the *y*-axis, the compound maintains E_g values within the range of 1–4 eV across various levels of tensile and compressive strain. This suggests that the compound is likely capable of preserving its semiconducting properties under applied strain. In addition, it has been observed that for both compressive and tensile strain, E_g values decrease with increase in strain. The fluctuating lattice parameter is largely responsible for the modulated band gaps, which are obtained by tweaking the valence band maximum (VBM) and conduction band minimum (CBM).[2]

The E_g values under varying tensile and compressive strain, as presented in Tables 3 and 4, reveal a notably consistent and gradual trend along the *x*-axis. Under tensile strain, the E_g values along the *x*-direction decrease progressively from 2.4751 eV (2%), 2.0100 eV (4%), and 1.4489 eV (6%). In contrast, the changes in E_g along the *y*- and *z*-axes are more abrupt and less predictable, for instance, a sharp drop to 0.1865 eV at 6% tensile strain in the *y*-direction suggests potential structural instability or electronic state disruptions.

Similarly, for compressive strain, the *x*-axis again shows a relatively steady trend, with E_g values increasing modestly from 2.8138 eV (unstrained) to 2.9221 eV (2%), 2.8602 eV (4%), and 2.7748 eV (6%). In contrast, the *y*-axis exhibit irregularities, such as a significant drop in E_g to 2.1509 eV at 6% compression along the *y*-axis, indicating non-linear or less stable responses to strain.

The observed band gap narrowing under tensile strain can be attributed primarily to lattice expansion, which reduces orbital overlap and leads to a downward shift of the CBM and/or an upward shift of the VBM. In contrast, compressive strain enhances orbital interactions and crystal-field splitting, generally pushing the CBM upward relative to the VBM and resulting in band gap widening. To further elucidate the structural origin of this behavior, the evolution of Sn–Cl bond lengths and internal Cl–Sn–Cl bond angles have been analyzed (Table S3 of SI). A systematic variation in bond length is observed, increasing from 2.4745 Å at 0% strain to 2.4792 Å under 6% tensile strain, and decreasing to 2.4657 Å under 6% compressive strain. This bond length modulation directly governs the overlap between Sn-5s/5p and Cl-3p orbitals, with elongation weakening and compression strengthening the hybridization. In addition, the *cis*-Cl–Sn–Cl bond angles remain close to 90° (90.328–90.729°), while the trans angles remain nearly linear (~180°) across all strain conditions, indicating that the $[SnCl_6]$ octahedra retain a near-ideal geometry with negligible angular distortion. These results confirm that bond length variation is the dominant structural factor governing the strain-induced electronic changes, while octahedral distortion plays a minimal role. The directional dependence of these effects explains the distinct and, in some cases, non-monotonic trends observed along different crystallographic axes.

Table 1 Lattice parameters and unit cell volume of the material with different levels of tensile strain

		Edge length (Å)			Edge angle (°)	Unit cell
Percentage of strain	e_{axis}	*a*	*b*	*c*	$\alpha = \beta = \gamma$	Volume (Å^3)
0%		7.5029	14.6936	7.3886	90	814.5533
2%	e_x	7.6530	14.6936	7.3886	90	830.8490
	e_y	7.5029	14.9875	7.3886	90	830.8460
	e_z	7.5029	14.6936	7.5364	90	830.8475
4%	e_x	7.8030	14.6936	7.3886	90	847.1337
	e_y	7.5029	15.2813	7.3886	90	847.1330
	e_z	7.5029	14.6936	7.6841	90	847.1306
6%	e_x	7.9531	14.6936	7.3886	90	863.4294
	e_y	7.5029	15.5752	7.3886	90	863.4256
	e_z	7.5029	14.6936	7.8319	90	863.4248

Table 2 Lattice parameters and unit cell volume of the material with different levels of compressive strain

Percentage of strain	e_{axis}	Edge length (Å)			Edge angle (°)	Unit cell
		a	b	c	$\alpha = \beta = \gamma$	Volume (Å^3)
0%		7.5029	14.6936	7.3886	90	814.5533
2%	e_x	7.3528	14.6936	7.3886	90	798.2577
	e_y	7.5029	14.3997	7.3886	90	798.2607
	e_z	7.5029	14.6936	7.2408	90	798.2592
4%	e_x	7.2028	14.6936	7.3886	90	781.9729
	e_y	7.5029	14.1059	7.3886	90	781.9736
	e_z	7.5029	14.6936	7.0931	90	781.9761
6%	e_x	7.0527	14.6936	7.3886	90	765.6773
	e_y	7.5029	13.8120	7.3886	90	765.6810
	e_z	7.5029	14.6936	6.9453	90	765.6819

Spin-orbit coupling (SOC) has been included to ensure a physically complete description of the electronic structure under strain. As shown in Tables 3 and 4, the inclusion of SOC leads to only a marginal reduction in the band gap values compared to non-SOC calculations, indicating a moderate SOC strength in the present lead-free halide perovskite. However, SOC consistently modifies the relative positions of the CBM and VBM, particularly under applied tensile and compressive strain. These SOC-induced shifts become relevant when lattice distortion alters orbital hybridization and anisotropic electronic responses along different crystallographic directions. Therefore, although the quantitative change in the band gap is small, inclusion of SOC is essential for accurately capturing strain-dependent band-edge evolution and ensuring reliable electronic property predictions.

Moreover, the uniform modulation of electronic properties along the x-axis suggests a more stable and predictable response to applied strain, making it a suitable direction for further investigations. Therefore, to ensure a focused and systematic analysis of strain effects on the optoelectronic and photovoltaic behavior of $(DMA)_2SnCl_6$, we have chosen to apply subsequent strains exclusively along the x-axis.

Furthermore, as depicted in Fig. S1, the band structures of the designed compound under different levels of strain are presented to support the reported band gap values. Fig. S1 reveals that at 0% of strain the direct band gap lies at the S-symmetry point. However, with the application of the strain, direct band gap moves to the Γ-symmetry point. This shift arises because strain engineering modifies the lattice constants and symmetry, thereby altering the electronic band structure through changes in orbital overlap and crystal field splitting.

3.3 Mechanical properties

Elastic constants are fundamental for predicting a crystal's response to external forces and assessing its mechanical stability. For orthorhombic systems, stability is governed by the

Table 3 Calculated band gap (E_g) values of $(DMA)_2SnCl_6$ with varying tensile strain

Percentage of strain	Non-SOC/SOC	e_{axis}	CBM (eV)	VBM (eV)	E_g (eV)
0%	Non-SOC		2.4278	−0.3860	2.8138
	SOC		2.4242	−0.3874	2.8116
2%	Non-SOC	e_x	2.0381	−0.4370	2.4751
		e_y	1.4083	−0.1069	1.5152
		e_z	1.2969	0.0358	1.2611
	SOC	e_x	2.0348	−0.4383	2.4731
		e_y	1.7788	−0.2734	2.0522
		e_z	2.1138	−0.4468	2.5606
4%	Non-SOC	e_x	1.6421	−0.3679	2.0100
		e_y	1.1470	0.0727	1.0743
		e_z	1.8322	−0.4318	2.2640
	SOC	e_x	1.6388	−0.3694	2.0082
		e_y	1.1439	0.0714	1.0725
		e_z	1.8287	−0.4332	2.2619
6%	Non-SOC	e_x	1.1475	−0.3014	1.4489
		e_y	0.2284	0.0419	0.1865
		e_z	1.0515	−0.5040	1.5555
	SOC	e_x	1.1444	−0.3015	1.4459
		e_y	0.2259	0.0405	0.1854
		e_z	1.0478	−0.5056	1.5534

Table 4 Calculated band gap (E_g) values of $(DMA)_2SnCl_6$ with varying compressive strain

Percentage of strain	Non-SOC/SOC	e_{axis}	CBM (eV)	VBM (eV)	E_g (eV)
0%	Non-SOC		2.4278	−0.3860	2.8138
	SOC		2.4242	−0.3874	2.8116
2%	Non-SOC	e_x	2.6926	−0.2295	2.9221
		e_y	2.7170	−0.1263	2.8433
		e_z	2.6846	−0.2056	2.8902
	SOC	e_x	2.6890	−0.2309	2.9199
		e_y	2.7133	−0.1277	2.8410
		e_z	2.6906	−0.2053	2.8959
4%	Non-SOC	e_x	2.8415	−0.0187	2.8602
		e_y	2.8760	0.3386	2.5374
		e_z	2.8267	−0.0056	2.8323
	SOC	e_x	2.8378	−0.0200	2.8578
		e_y	2.8723	0.3372	2.5351
		e_z	2.8230	−0.0069	2.8299
6%	Non-SOC	e_x	2.9918	0.2170	2.7748
		e_y	3.0410	0.8901	2.1509
		e_z	3.0961	0.3531	2.7430
	SOC	e_x	2.9881	0.2157	2.7724
		e_y	3.0373	0.8883	2.1490
		e_z	3.0924	0.3518	2.7406

Table 5 Strain-dependent effective mechanical parameters of $(DMA)_2SnCl_6$ under tensile deformation, including elastic-related coefficients C_{ij} (kbar), bulk modulus (B) (kbar), shear modulus (G) (kbar), Young's modulus (Y) (kbar), Pugh's ratio (B/G), and Poisson's ratio (n)

Elastic parameters (kbar)	Percentage of strain			
	0%	2%	4%	6%
C_{11}	25.96	39.75	37.89	32.18
C_{12}	−5.54	20.15	26.64	28.76
C_{13}	−89.75	39.25	28.99	22.07
C_{22}	59.63	97.17	88.74	82.79
C_{23}	30.33	46.79	47.43	44.88
C_{33}	214.75	271.46	272.97	264.75
C_{44}	14.57	24.03	16.75	17.28
C_{55}	−9.77	12.48	4.40	1.26
C_{66}	21.19	50.47	43.48	37.23
B	22.60	50.25	51.97	48.80
G	63.66	29.39	22.18	17.52
Y	94.30	73.68	58.03	46.05
B/G	0.36	1.71	2.34	2.79
n	−0.26	0.25	0.31	0.31

Born criteria: $C_{11} > 0$; $C_{11}C_{22} > {C_{12}}^2$; $C_{11}C_{22}C_{33} + 2C_{12}C_{13}C_{23} - C_{11}{C_{23}}^2 - C_{22}{C_{13}}^2 - C_{33}{C_{12}}^2 > 0$; $C_{44} > 0$; $C_{55} > 0$; $C_{66} > 0$.[33] Using finite strain theory in the thermo_pw package of QE, the elastic constants of the equilibrium (unstrained) orthorhombic perovskite have been evaluated and are found to satisfy the Born stability criteria, confirming its mechanical stability at equilibrium. To further examine the influence of external deformation, the evolution of elastic-related mechanical parameters under tensile and compressive strain have also been analyzed and is summarized in Table 5 and 6, respectively. It should be emphasized that elastic constants and derived moduli are rigorously defined only within the linear elastic regime around the equilibrium structure. Therefore, the strain-dependent quantities reported here are interpreted as effective mechanical descriptors under finite deformation, rather than true equilibrium elastic constants.

Table 6 Strain-dependent effective mechanical parameters of $(DMA)_2SnCl_6$ under compressive deformation, including elastic-related coefficients C_{ij} (kbar), bulk modulus (B) (kbar), shear modulus (G) (kbar), Young's modulus (Y) (kbar), Pugh's ratio (B/G), and Poisson's ratio (n)

Elastic parameters (kbar)	Percentage of strain			
	0%	2%	4%	6%
C_{11}	25.96	132.92	138.35	134.16
C_{12}	−5.54	154.52	73.01	75.47
C_{13}	−89.75	52.39	48.74	48.25
C_{22}	59.63	173.26	157.20	143.58
C_{23}	30.33	55.90	48.43	43.04
C_{33}	214.75	286.96	302.11	296.07
C_{44}	14.57	13.56	16.01	29.60
C_{55}	−9.77	31.83	31.99	32.62
C_{66}	21.19	79.95	78.05	75.91
B	22.60	536.44	104.08	98.51
G	63.66	39.41	44.34	48.01
Y	94.30	109.78	115.91	123.70
B/G	0.36	13.61	2.35	2.05
n	−0.26	0.39	0.31	0.29

In addition, elastic moduli of the intended compound have been evaluated *via* the Voigt–Reuss–Hill (VRH) approximation. Shear modulus (G) reflects resistance to shape change, Young's modulus (Y) indicates stiffness, and Pugh's ratio (B/G) and Poisson's ratio (n) distinguish ductility from brittleness (thresholds: $B/G > 1.75$, $n > 0.26$). The relatively low Y values suggest enhanced mechanical compliance under deformation. Furthermore, the strain-dependent trends in the Pugh's ratio (B/G) and Poisson's ratio (n) qualitatively indicate a tendency toward ductile-like mechanical response under moderate tensile and compressive deformation.[34–36] This apparent ductile behavior, as inferred from the Pugh's ratio and Poisson's ratio, is noteworthy because strongly covalent solids are classically associated with intrinsic brittleness, whereas metallic systems often display substantial plastic deformability. The present compound, however, exhibits a mixed bonding character rather than purely covalent bonding. Directional covalent bonds provide structural stability and strength, while the presence of more delocalized and partially metallic/ionic interactions reduces bond directionality and can facilitate defect motion and lattice relaxation under load. The combination of these bonding motifs can therefore reconcile the elastic criteria ($B/G > 1.75$, $n > 0.26$) with the expected mechanical response, indicating that the material behaves as a ductile mixed-bonding solid rather than as a strictly brittle covalent crystal.[37–39]

Overall, while elastic stability is established at equilibrium, strain engineering significantly modifies the mechanical response of the perovskite. No mechanical instability is observed within the investigated strain range, highlighting its potential for strain-tolerant and flexible device applications.

3.4 Optical properties

To investigate the optical characteristics of the selected compound $(DMA)_2SnCl_6$, we have computed the complex dielectric functions (ε) for the mentioned compound using epsilon.x post processing code available in QE software. ε mainly consist of two parts: real (ε_1) and imaginary (ε_2), which can be represented as:[40]

$$\varepsilon(\omega) = \varepsilon_1(\omega) + i\varepsilon_2(\omega). \quad (6)$$

ε can be used to illustrate the coulombic interaction between an electron and a hole. When ε is increased, the interaction between electron and hole decreases, thereby reducing the exciton binding energy to speed up the charge separation. The high value of ε indicates that the material can retain a large amount of charge for an extended period of time, which improves the material's performance. The real part of complex dielectric function, *i.e.*, ε_1 represents the polarization induced in the material. On the other hand, the imaginary part, *i.e.*, ε_2 measures the loss of radiation energy. In addition, ε_1 measures the difference in wavelength between the electromagnetic spectrum and vacuum, while ε_2 measures the material's absorption.[40–42]

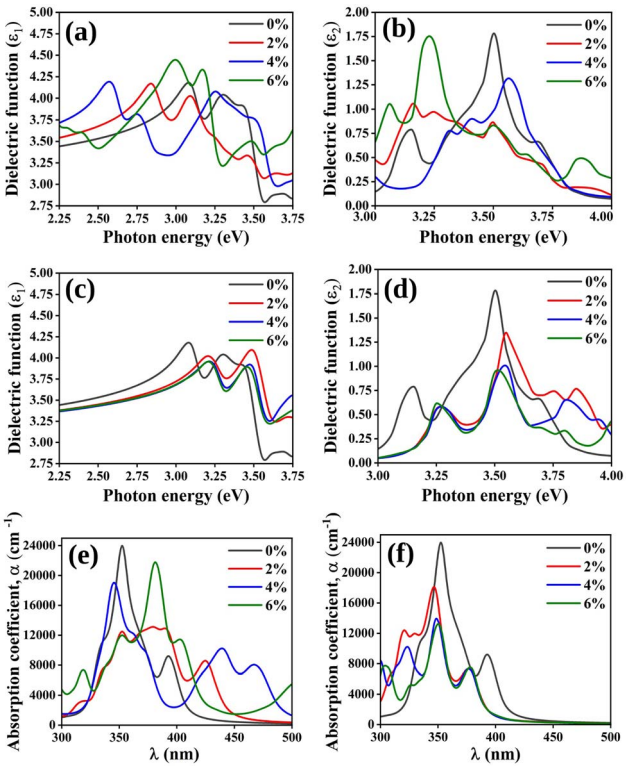

Fig. 2 Plot of (a) real(ε_1) and (b) imaginary(ε_2) parts of dielectric functions of $(DMA)_2SnCl_6$ on varying tensile strain, and (c) real(ε_1) and (d) imaginary(ε_2) parts of dielectric functions of $(DMA)_2SnCl_6$ on varying compressive strain, and (e) and (f) are the UV-Visible spectra of $(DMA)_2SnCl_6$ on varying tensile and compressive strain, respectively.

Furthermore, ε_1 and ε_2 are interconnected *via* the Kramers–Kronig relation,[43] which follow:

$$\varepsilon_1(\omega) = 1 + \frac{2}{\pi} P \int_0^{\infty} \frac{\omega' \varepsilon_2(\omega')}{\omega'^2 - \omega^2} \mathrm{d}\omega', \tag{7}$$

In this context, P indicates the Cauchy principal value, and the ε_2 appeared in the above equation can be calculated from direct interband transitions using the Fermi Golden Rule, as given below :[43,44]

$$\varepsilon_2(\hbar\omega) = \frac{2e^2\pi}{\Omega\varepsilon_0} \sum_{\kappa,c,v} |\langle \psi_\kappa{}^c | \hat{\mu} \cdot r | \psi_\kappa{}^v \rangle|^2 \delta(E_\kappa{}^c - E_\kappa{}^v - \hbar\omega). \tag{8}$$

Table 7 Calculated V_{oc}, J_{sc}, and η values of $(DMA)_2SnCl_6$ with varying tensile strain

Percentage of strain	E_g (eV)	E_{loss} (eV)	V_{oc} (eV)	J_{sc} (A m^{-2})	η (%)
0%	2.8138	0.7	2.1138	29.84	6.31
	2.8138	0.5	2.3138	29.84	6.90
2%	2.4751	0.7	1.7751	64.87	11.51
	2.4751	0.5	1.9751	64.87	12.81
4%	2.0100	0.7	1.3100	143.38	18.78
	2.0100	0.5	1.5100	143.38	21.64
6%	1.4489	0.7	0.7489	308.65	23.11
	1.4489	0.5	0.9489	308.65	29.28

Table 8 Calculated V_{oc}, J_{sc}, and η values of $(DMA)_2SnCl_6$ with varying compressive strain

Percentage of strain	E_g (eV)	E_{loss} (eV)	V_{oc} (eV)	J_{sc} (A m^{-2})	η
0%	2.8138	0.7	2.1138	29.84	6.31
	2.8138	0.5	2.3138	29.84	6.90
2%	2.9221	0.7	2.2221	23.20	5.15
	2.9221	0.5	2.4221	23.20	5.62
4%	2.8602	0.7	2.1602	26.71	5.77
	2.8602	0.5	2.3602	26.71	6.30
6%	2.7748	0.7	2.0748	32.84	6.81
	2.7748	0.5	2.2748	32.84	7.47

Here, Ω, ψ, μ, ω, and r correspond to the unit cell volume, wavefunctions, external field vector, photon frequency, and momentum operator, respectively. Additionally, c and v denote the unoccupied and occupied states within reciprocal space at the κ point.

The computed real and imaginary parts of dielectric function of the selected compound are provided in Fig. 2(a–d). Fig. 2 manifests that the designed compound exhibits maximum value within the visible region of the electromagnetic spectrum.

Furthermore, the absorption coefficient (α) of the compound, which is related to the optical absorption ability, has been calculated from ε_1 and ε_2 according to the following equation:[43,44]

$$\alpha(\omega) = \sqrt{2}\omega \sqrt{-\varepsilon_1(\omega) + \sqrt{\varepsilon_1{}^2(\omega) + \varepsilon_2{}^2(\omega)}}. \tag{9}$$

The UV-Vis spectra of the designed compound are presented in Fig. 2(e and f). As shown in the figure, the intended compound exhibits strong absorption in the near UV region of the electromagnetic (EM) spectrum at various level of applied strain.

The red shift under 2% and 6% tensile strain (Fig. 2e) arises from Sn–Cl bond elongation and lattice expansion, which weaken orbital overlap and slightly narrow the bandgap. This lowers the excitation energy, shifting the absorption edge to longer wavelengths. The small shift, along with nearly unchanged dielectric functions, shows that $(DMA)_2SnCl_6$ retains its near-UV absorption and remains stable under mechanical strain, benefiting robust optoelectronic applications.

3.5 Photovoltaic performance

To investigate the photovoltaic features of the selected compound, we have estimated the open circuit voltage (V_{oc}), short-circuit current density (J_{sc}), and theoretical power conversion efficiency (η) of varying tensile and compressive strains. The obtained results are reported in the Tables 7 and 8, respectively. These tables demonstrate that, in most of the cases, the value of J_{sc} increases with the increase in percentage of strain. Consequently, $(DMA)_2SnCl_6$ shows the highest value of PCE (η) 29.28% and 7.47% in case of 6% tensile and compressive strain, respectively.

The improvement in J_{sc} and PCE under tensile strain can be attributed to lattice expansion, which might reduces the carrier effective mass, thereby enhancing mobility, while compressive strain has the opposite effect, leading to reduced efficiency. This strain-dependent asymmetry highlights that tensile deformation can act as an effective tool to engineer the optoelectronic properties of $(DMA)_2SnCl_6$, making it a promising candidate for strain-tunable, high-performance photovoltaic devices.

4 Conclusion and future outlook

Herein, we have provided a comprehensive analysis of the impact of applied strain on the optoelectronic and photovoltaic properties of $(DMA)_2SnCl_6$, utilizing DFT calculations. The obtained band gap values for the studied compound indicate its potential as a promising candidate for photovoltaic applications. Notably, under variation of both tensile and compressive strain, the band gap exhibits a decreasing trend with increasing strain. This modulation in the band gap is primarily attributed to variations in the lattice parameters, which influence the positioning of the valence band maximum (VBM) and conduction band minimum (CBM).

Furthermore, an in-depth mechanical stability analysis confirms that the designed compound satisfies most of the Born stability criteria, thereby ensuring its structural integrity under different magnitudes and types of strain. Besides that, the optical absorption coefficient analysis reveals that $(DMA)_2SnCl_6$ exhibits a maximum absorption in the near-UV region of the EM spectrum. From a photovoltaic application standpoint, the strain-induced modulation of dielectric response, absorption behavior, and band gap in $(DMA)_2SnCl_6$ directly translates into tunable device-relevant parameters. In particular, tensile strain leads to a red-shifted absorption edge and increased absorption coefficient, resulting in a substantial enhancement of the short-circuit current density. These effects collectively explain the observed improvement in theoretical power conversion efficiency, with a maximum PCE of 29.28% achieved under 6% tensile strain applied along the x-axis. This highlights strain engineering as a viable and effective strategy for optimizing hybrid double perovskites toward efficient and environmentally benign photovoltaic applications.

Looking ahead, strain-engineered lead-free double perovskites represent a promising frontier in sustainable optoelectronics, where future research should focus on bridging computational predictions with experimental realization and device-level optimization. Expanded studies on strain modulation may unlock enhanced stability and efficiency beyond current limits. In this context, computational advances particularly machine learning (ML) frameworks such as XGBoost offer significant potential for high-throughput screening of lead-free double perovskites. These approaches enable rapid prediction of key photovoltaic descriptors, including optimal band gaps in the range of 1.3–1.4 eV and low formation energies, as demonstrated for candidates such as Cs_2YAgBr_6 and $Cs_2AgSbBr_6$. Compared to conventional DFT, ML-driven models efficiently explore vast compositional and strain-responsive design spaces, identifying materials with direct band gaps suitable for solar cell applications. Furthermore, integrating many-body techniques such as GW and Bethe–Salpeter equation (BSE) methods with ML models will allow more accurate treatment of quasiparticle energies and excitonic effects under strain, which is crucial for reliable prediction of luminescence and photovoltaic performance.[45–48]

Overall, this study highlights the pivotal role of strain engineering in modulating the functional properties of lead-free double halide perovskites and provides a roadmap for future computational and experimental efforts toward next-generation, environmentally benign photovoltaic technologies.

Author contributions

Tanmoy Kalita: conceptualization; data curation; formal analysis; investigation; methodology; software; validation; visualization; writing/original draft preparation. Manjet Rajak: formal analysis; investigation; software. Dhruba Jyoti Kalita: funding acquisition; project administration; resources; supervision; writing/review & editing.

Conflicts of interest

There are no conflicts to declare.

Data availability

The data that support the findings of this study are available within the article and its supplementary information (SI). Supplementary information: the calculated lattice parameters and band gap values of the reference perovskite material, along with the computed band structures and optimized atomic coordinates of the studied compound under varying levels of applied strain, are provided in the SI. Additionally, the evolution of Sn–Cl bond lengths and Cl–Sn–Cl bond angles with strain, as well as the variation of total energy (in Ry) as a function of applied strain, are also included. See DOI: https://doi.org/10.1039/d6ra02285e.

Acknowledgements

The authors gratefully acknowledge the Department of Science and Technology, India (SB/FT/CS-077/2013; CRG/2022/001313) for financial support. The authors also extend their gratitude to the University Grants Commission for the UGC-BSR Research Start-Up Grant (NO.F.30.-122/2015(BSR)) and to Gauhati University for providing research facilities and additional financial support. In addition, the author Mr Tanmoy Kalita acknowledges the Council of Scientific & Industrial Research (CSIR), Government of India, for awarding the SRF-DIRECT fellowship (File No.: 09/0059(23727)/2025-EMR-I).

Notes and references

1 E. Meyer, D. Mutukwa, N. Zingwe and R. Taziwa, *Metals*, 2018, **8**, 667.

2 M. Javed, M. A. Sattar, M. Benkraouda, N. Amrane and A. Najar, *Appl. Surf. Sci.*, 2023, **627**, 157244.
3 J. Wu, S.-C. Liu, Z. Li, S. Wang, D.-J. Xue, Y. Lin and J.-S. Hu, *Natl. Sci. Rev.*, 2021, **8**, nwab047.
4 T. Liu, Y. Zong, Y. Zhou, M. Yang, Z. Li, O. S. Game, K. Zhu, R. Zhu, Q. Gong and N. P. Padture, *Chem. Mater.*, 2017, **29**, 3246–3250.
5 X. Shai, W. Chen, J. Sun, J. Liu and J. Chen, *Small Sci.*, 2023, **3**, 2300014.
6 M. F. Rahman, M. Harun-Or-Rashid, M. R. Islam, A. Ghosh, M. K. Hossain, S. Bhattarai, R. Pandey, J. Madan, M. Ali and A. B. M. Ismail, *Phys. Scr.*, 2023, **98**, 115105.
7 M. R. Islam, A. Zahid, M. A. Rahman, M. F. Rahman, M. Islam, M. K. Hossain, M. Ali, M. A. Iqbal, F. I. Bakhsh and S. Ahmad, *J. Phys. Chem. Solids*, 2024, **184**, 111722.
8 X.-H. Zhao, F. Wang, D.-Y. Hu, L.-M. Lu, L. Li, T.-Y. Tang and Y.-L. Tang, *J. Mol. Model.*, 2022, **28**, 337.
9 L.-K. Gao, Y.-L. Tang and X.-F. Diao, *Appl. Sci.*, 2020, **10**, 5055.
10 L. A. Muscarella and E. M. Hutter, *ACS Energy Lett.*, 2022, **7**, 2128–2135.
11 S. Ghosh, H. Shankar and P. Kar, *Mater. Adv.*, 2022, **3**, 3742–3765.
12 F. Ji, G. Boschloo, F. Wang and F. Gao, *Sol. RRL*, 2023, **7**, 2201112.
13 A. Boubekraoui, M. Ziati and H. Ez-Zahraouy, *Comput. Theor. Chem.*, 2022, **1215**, 113833.
14 P. Giannozzi, S. Baroni, N. Bonini, M. Calandra, R. Car, C. Cavazzoni, D. Ceresoli, G. L. Chiarotti, M. Cococcioni, I. Dabo, *et al.*, *J. Phys. Condens. Matter*, 2009, **21**, 395502.
15 S. Gražulis, D. Chateigner, R. T. Downs, A. Yokochi, M. Quirós, L. Lutterotti, E. Manakova, J. Butkus, P. Moeck and A. Le Bail, *J. Appl. Cryst.*, 2009, **42**, 726–729.
16 A. Jain, S. P. Ong, G. Hautier, W. Chen, W. D. Richards, S. Dacek, S. Cholia, D. Gunter, D. Skinner, G. Ceder, *et al.*, *APL Mater.*, 2013, **1**, 011002.
17 P. Ziesche, S. Kurth and J. P. Perdew, *Comput. Mater. Sci.*, 1998, **11**, 122–127.
18 J. P. Perdew, K. Burke and M. Ernzerhof, *Phys. Rev. Lett.*, 1996, **77**, 3865.
19 C. Adamo and V. Barone, *J. Chem. Phys.*, 1999, **110**, 6158–6170.
20 J. P. Perdew, A. Ruzsinszky, G. I. Csonka, O. A. Vydrov, G. E. Scuseria, L. A. Constantin, X. Zhou and K. Burke, *Phys. Rev. Lett.*, 2008, **100**, 136406.
21 J. Heyd and G. E. Scuseria, *J. Chem. Phys.*, 2004, **121**, 1187–1192.
22 M. M. Hossain, M. A. Ali, M. M. Uddin, S. H. Naqib and A. A. Islam, *ACS Omega*, 2021, **6**, 33899–33913.
23 M. Ali and A. Islam, *Phys. B: Condens. Matter*, 2012, **407**, 1020–1026.
24 M. Ali, M. Roknuzzaman, M. Nasir, A. Islam and S. Naqib, *Int. J. Mod. Phys. B*, 2016, **30**, 1650089.
25 F. Heidari Gourji and D. Velauthapillai, *Molecules*, 2021, **26**, 2010.
26 M. R. Filip, S. Hillman, A. A. Haghighirad, H. J. Snaith and F. Giustino, *J. Phys. Chem. Lett.*, 2016, **7**, 2579–2585.
27 J. Even, L. Pedesseau, J.-M. Jancu and C. Katan, *J. Phys. Chem. Lett.*, 2013, **4**, 2999–3005.
28 Y. Cai, W. Xie, H. Ding, Y. Chen, K. Thirumal, L. H. Wong, N. Mathews, S. G. Mhaisalkar, M. Sherburne and M. Asta, *Chem. Mater.*, 2017, **29**, 7740–7749.
29 Y. Yu, D. Zhao, C. R. Grice, W. Meng, C. Wang, W. Liao, A. J. Cimaroli, H. Zhang, K. Zhu and Y. Yan, *RSC Adv.*, 2016, **6**, 90248–90254.
30 J. Chang, L. Jiang, G. Wang, W. Zhao, Y. Huang and H. Chen, *Phys. Chem. Chem. Phys.*, 2021, **23**, 14449–14456.
31 D. Liu, Q. Li, J. Hu, R. Sa and K. Wu, *J. Phys. Chem. C*, 2019, **123**, 12638–12646.
32 L. Yu and A. Zunger, *Phys. Rev. Lett.*, 2012, **108**, 068701.
33 F. Mouhat and F.-X. Coudert, *Phys. Rev. B*, 2014, **90**, 224104.
34 K. M. Hossain, M. Z. Hasan and M. L. Ali, *AIP Adv.*, 2021, **11**, 015052.
35 M. Roknuzzaman, K. Ostrikov, H. Wang, A. Du and T. Tesfamichael, *Sci. Rep.*, 2017, **7**, 14025.
36 L. Liu, L. Lian and J. Yu, *Mater. Res.*, 2019, **22**, e201800624.
37 S. Shakeel, P. Song, S. H. Shah, Z. Zada, T. Huang, A. Laref, N. Hakimi and M. Faizan, *Mater. Chem. Phys.*, 2024, **324**, 129683.
38 F. Moitzi, D. Şopu, D. Holec, D. Perera, N. Mousseau and J. Eckert, *Acta Mater.*, 2020, **188**, 273–281.
39 H. Niu, X.-Q. Chen, P. Liu, W. Xing, X. Cheng, D. Li and Y. Li, *Sci. Rep.*, 2012, **2**, 718.
40 T. Chutia and D. J. Kalita, *RSC Adv.*, 2022, **12**, 25511–25519.
41 Y. Dong, R. Zhu and Y. Jia, *J. Phys. Chem. C*, 2021, **125**, 14883–14890.
42 Q. Lin, A. Armin, R. C. R. Nagiri, P. L. Burn and P. Meredith, *Nat. Photonics*, 2015, **9**, 106–112.
43 J. Chang, H. Chen, H. Yuan, B. Wang and X. Chen, *Phys. Chem. Chem. Phys.*, 2018, **20**, 941–950.
44 D. Liu, Q. Li, J. Hu, H. Jing and K. Wu, *J. Mater. Chem. C*, 2019, **7**, 371–379.
45 P. Phonglamjiakngam, Z. A. Hazaea, M. Wang and N. Pootrakulchote, *Sol. Energy*, 2026, **303**, 114164.
46 S. K. Fatima, R. H. Alzard, R. Amna, M. H. Alzard, K. Zheng and M. Abdellah, *Mater. Adv.*, 2025, **6**, 7634–7661.
47 J. Wang, Y. Wang, X. Liu and X. Wang, *Molecules*, 2025, **30**, 2378.
48 S. Singh, P. K. Nayak, S. Tretiak and D. Ghosh, *J. Phys. Chem. Lett.*, 2023, **14**, 9479–9489.